University of Jyväskylä

Masters Thesis

Analysis of the charge state distribution produced in a ^{78}Kr + ^{98}Mo fusion evaporation reaction utilizing the MARA separator

Alexandra Lightfoot

supervised by
Dr. Jan sarén

October 23, 2016

Abstract

Experimental results on the charge state distribution of the fusion evaporation reaction $^{78}\mathrm{Kr} + {}^{98}\mathrm{Mo}$ are presented. The data has been taken from the 1st commissioning run of MARA (Mass Analysing Recoil Apparatus). Data from the charge states of $q = 29 - 33$ were collected. Here, q represents the elementary charge describing the number of electrons removed from a neutral atom. Results show an expected gaussian distribution around the most probable charge, $\bar{q}$. A most probable charge state of $\bar{q} = (27.99 \pm 0.20)$ was obtained after fitting the data. The value of $\bar{q}$ was lower than initially anticipated, which was mainly a result of a less than desired beam energy delivered on the day of testing.

Contents

1 Introduction and motivation **6**

2 Introduction to nuclear reactions **8**

3 Fusion evaporation reactions **10**

3.1 The compound nucleus 10

3.2 Reaction kinematics 13

3.2.1 Excitation energy 16

3.3 Evaporated particle distribution 17

3.4 Angular distribution and acceptance 18

3.4.1 Aside on barriers 20

4 Target interactions **22**

4.1 Charge state distribution 22

4.2 Energy loss 23

5 Instrumentation - MARA **27**

5.1 Main components and mathematics 27

5.2 Focal plane 31

5.2.1 Detectors 31

5.2.2 Mass focal plane 32

6 Data acquisition and analysis **34**

6.1 Identification of charge states and masses 37

6.1.1 Reference charge 38

6.1.2 Reference mass, parameter settings and calculations 39

7 Results **41**

7.1 Calculation of energy losses 41

7.2 Charge state distribution 42
7.2.1 Errors 45

8 Discussion **46**

9 Conclusion **48**

List of Figures

2.1 Different types of nuclear reactions including: elastic scattering, inelastic scattering, fusion and DIS, can occur depending on the energy of the projectile and value of the impact parameter, b. 9

3.1 Formation and decay sequence for a compound nucleus. The CN first emits particles until it is no longer energetically possible. Further de-excitation is followed by the emission of gamma rays until it reaches the ground state. . 11

3.2 Some of the possible decay channels for a ^{78}Kr beam impinged on a ^{98}Mo target. 11

3.3 Cross section for different masses produced in the reaction of ^{78}Kr and ^{98}Mo as simulated by the program PACE4. The total cross section of all recoil products is highlighted in red. The energy of the beam is given as in the laboratory frame. 12

3.4 Energy distributions in CoM of evaporated particles after a ^{78}Kr on ^{98}Mo reaction at $E_{\mathrm{k,lab}} = 357$ MeV as simulated by PACE4 18

4.1 Schematic showing that the target is some finite thickness, which both the projectile and recoil nucleus must traverse through. Different locations of the CN composition depict how much kinetic energy the final recoil has after the target. 25

5.1 Layout of MARA. The optical element on the left, consisting of $\mathrm{Q}_1, \mathrm{Q}_2$ and Q_3 is the quadrupole triplet. Recoils are bent according to the electrostatic deflector and magnetic dipoles. They are brought to focus at the transmission detector in the focal plane. 28

5.2 Schematic showing the tilted mass focal plane, and how the particles would look in phase space. Only the reference particle will deposit its energy centrally on the MWPC detector. 32

6.1 User interface for Grain and histogram of Energy [MeV] vs. ToF[ns], for all recoils entering the focal plane. The colour scale in the right of the image signifies the amount of recoils - going from blue, indicating no recoils, to red. 34
6.2 Zoomed in shot of Energy [MeV] vs. ToF [ns] histogram, giving an example of how gating is set on the recoil particles (highlighted in yellow) 35
6.3 Recoils separated by charge after a sorting code is applied to a saved gate file 36
6.4 Sketch similar to that shown in figure 6.3 with labelled charge distributions and how they are shifted with respect to the reference charge. It is also shown how the distance Δx_q was defined. 38

7.1 Plot to show how the energy of the recoil on exiting the target, is dependant on the depth in the target at which it was created. 41
7.2 Final charge state distribution for ^{78}Kr on^{98}Mo reaction at beam energy of 357 MeV. The distribution is fitted to a Gaussian function. 44

List of Tables

5.1 Optical properties of MARA 31

6.1 Calculated distance of charge states from $q_0 = 32.5$ as seen in the MWPC . 39
6.2 Atomic mass and atomic number of reaction, compound and reference elements 40
6.3 Parameter values at the Coulomb barrier and at 357 MeV beam energy . . 40

7.1 Raw number of counts taken from spectrum data for four different runs. Each run defines its reference charge in brackets. 43
7.2 The relative abundance of the higher charge with respect to the lower charge for each run. The run order follows the same as that in table 7.1. 43
7.3 Results from fitting a Gaussian function to the experimental data 45

1. Introduction and motivation

The understanding of nuclear reactions has occurred at a relatively fast pace since the early 1900's; with Rutherford simultaneously discovering the proton and initiating the first induced nuclear reaction in 1919 [1]. The experiment was constructed by bombarding alpha particles into a tube of gaseous ^{14}N to produce ^{17}C + proton.

Further development in nuclear research then came with Chadwick's discovery of the neutron in 1932; whilst in the same year, nuclear transformations via accelerating protons into atoms were produced by Cockroft and Walton [2]. In the subsequent years, the production of artificial radionuclides was pursued by many now well known scientists including Curie and Bohr; the latter of which began using neutrons instead of protons to induce nuclear reactions.

Thus it is clear, that the early 20th century lay the foundations of what nuclear research has developed into today, and since then, reactions of all different possible combinations have been used in an effort to produce not only new elements, but also understand nuclear shape and structure.

This master's thesis focuses on one specific type of nuclear reaction called a *fusion evaporation reaction*. Practically, the only way to produce heavy atoms with large atomic numbers (Z), is through fusion evaporation reactions. In this type of reaction two nuclei fuse together to form a compound nucleus in a highly excited state. The compound nucleus then decays via particle evaporation and gamma-ray emission, with the remaining nucleus (a *recoil*) available to be detected in order to examine its properties. This kind of reaction is induced by directing a beam of ions at a stationary target. A large proportion of the beam ions do not react with the target material at all, instead passing directly through it. In addition, not only one type of recoil is produced but many of varying masses and charge states. Therefore, the desired recoil needs to be separated from the unwanted beam ions and if possible, other recoils. Such separation can be achieved using a *mass spectrometer* at dedicated facilities such as MARA (Mass Analysing Recoil Apparatus) at JYFL (University

of Jyväskylä, Finland).

There are many different variations of separators comparable to MARA, that use similar optics to accomplish beam separation. In all separators the optics are defined by electric and magnetic fields. Some of these separators and spectrometers include the FMA (Argonne National Laboratory, Illinois, USA), the HRIBF RMS (Oak Ridge National Laboratory, USA), HIRA (Nuclear Science centre, India) and EMMA (TRIUMF, Canada). All use electrostatic deflectors to separate the beam ions from recoils. These separators have the additional property that they can disperse the recoils according to their mass to charge ratio. The most desirable separator is the one which can achieve maximum separation of the beam (and recoils) whilst maintaining a high recoil yield.

With electromagnetic fields, separation is performed either via the E_{k}/q or p/q ratios; where E_{k} is the kinetic energy, p is the momentum and q is the charge of the particle (recoil), which describes the number of electrons removed from the neutral atom. Thus it is clear that charge is an exceptionally important parameter to monitor, if the nuclei of interest are to be separated and detected successfully. The final charge state of the recoils is complicated to predict, but comes from interactions with atoms within the vicinity of the target. The motivation for this thesis comes from a need to determine the average charge state of a specific recoil, following the fusion evaporation reaction $^{78}\mathrm{Kr} + {}^{98}\mathrm{Mo}$, in order to maximise the recoil yield and efficiency of MARA. The results have been analysed from the first commissioning run of MARA, with the idea that the reaction itself can be considered as a benchmark from which it is easy to observe the correct tuning of the separator [3].

2. Introduction to nuclear reactions

In order to gain some insight to nuclear reactions, it is necessary to first introduce the notation used to describe them. A nuclear reaction is most commonly induced by a moving projectile (P) colliding with a target (T), which remains at rest. Such a reaction is described simply as:

$$\mathrm{P} + \mathrm{T} \longrightarrow \mathrm{R} + \mathrm{x}, \tag{2.1}$$

where R is the residual nucleus and x is usually some lighter emitted particle. The moving projectile consists of a beam of charged particles; anything from protons to heavy ions. The target can be a gas or solid and come in a variety of thicknesses. The shorthand notation for such a reaction is written as:

$$\mathrm{T(P,x)R}. \tag{2.2}$$

The total number of protons and neutrons in any nuclear reaction is always conserved.

Nuclear reactions can occur via different mechanisms dependant on the energy of the projectile and the value of it's *impact parameter* b, to the target nucleus. Some of these mechanisms are illustrated in figure 2.1. For example, using the notation defined above, if x and R nuclei are identical to T and P, then the reaction is called *elastic scattering*. In this scenario, the projectile moves close to the target nucleus, interacts with the nuclear field and changes direction, leaving the both the projectile and target nuclei in their ground state. Alternatively, *inelastic scattering* can occur which leaves either the projectile or target nucleus in an excited state.

If a projectile interacts with a specific nucleon of a target nucleus, with the nucleon leaving the nucleus, then it is deemed a *direct reaction*; having taken place in a single quick ($10^{-21}s$) event [4]. A nucleon can also be added to the target atom from the projectile. *Transfer reactions* are similar, but take place over a longer period of time and more nucleons may be transferred.

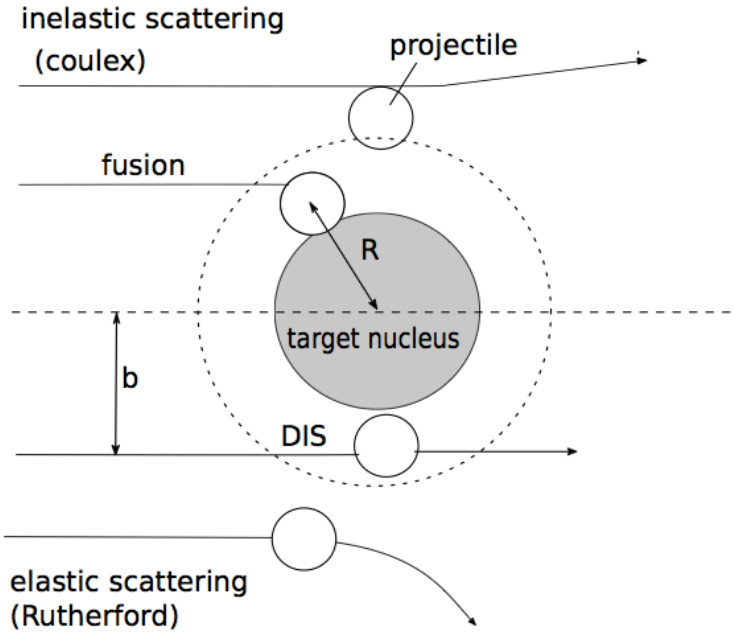

Figure 2.1: Different types of nuclear reactions including: elastic scattering, inelastic scattering, fusion and DIS, can occur depending on the energy of the projectile and value of the impact parameter, b.

"DIS" as written in the figure, stands for *deep inelastic scattering* and substantial energies are used in those types of reactions to look at the internal structure of nuclei.

Finally, fusion reactions can occur, where the nuclei of the beam and target fuse together to form a compound nucleus. Normally, this results in fission or particle evaporation. The latter is designated a *fusion evaporation reaction* and is the focus of study for this experiment. It should be noted that the number of reactions are not limited to those described here; where only the most common are briefly mentioned.

3. Fusion evaporation reactions

3.1. The compound nucleus

A compound nucleus (CN) is created when one of the projectiles in the ion beam hits a target nucleus in such a way that they fuse together to form a new particle. During formation, the energy and momentum of the projectile are shared amongst the nucleons of the target until statistical equilibrium is reached. This intermediate state can be incorporated into the general nomenclature for nuclear reactions and equation 2.1 becomes:

$$\mathrm{P} + \mathrm{T} \longrightarrow \mathrm{CN}^{*} \longrightarrow \mathrm{R} + \mathrm{x}. \tag{3.1}$$

Here, x is an evaporated particle, for example a proton, neutron, alpha particle or some combination of these, and R is the *recoil*. The recoil is the nucleus that remains after evaporation and de-excitation has taken place. Due to the high energy of the projectile, the CN is in a highly excited state after formation, and it becomes necessary for it to remove some of this excess energy. The asterisk denotes that the CN is in an excited state.

At approximately 10^{-19}s after formation [5], the CN starts to remove this excess energy through the most efficient way possible: particle emission (neutrons, protons and alpha particles). After particle emission, further decay occurs via cascades of gamma rays. Figure 3.1 shows a schematic of the typical processes for the creation and decay of a CN [5].

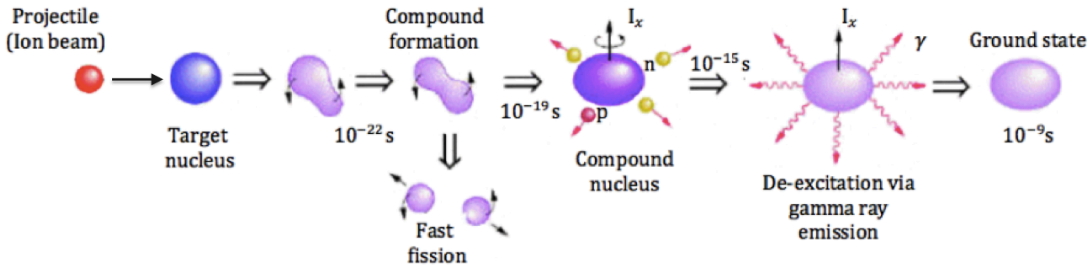

Figure 3.1: Formation and decay sequence for a compound nucleus. The CN first emits particles until it is no longer energetically possible. Further de-excitation is followed by the emission of gamma rays until it reaches the ground state.

The length of time the CN lives is considered long when compared with other types of reactions. Since the length of the reaction is long, it essentially forgets its history. This therefore demands that the CN lives longer than it would take a nucleon to traverse the nucleus i.e. the length of a direct reaction. These long lived reactions with formation of a CN are of particular interest for the study of nuclei in high spin states, which are a result of the large angular momentum transfer.

The CN can decay in several different ways called channels. The amount of energy available, as well as the angular momentum of the incident particle signifies what kind of particle evaporation is possible. Some of the possible decay channels for the reaction $^{78}\mathrm{Kr} + {}^{98}\mathrm{Mo}$ are shown in figure 3.2:

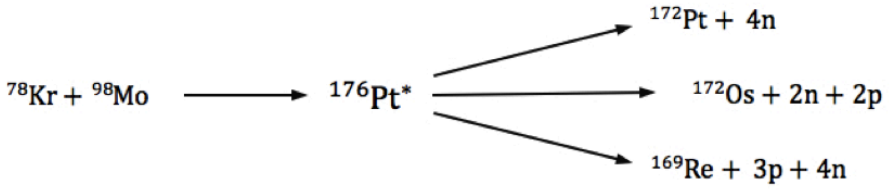

Figure 3.2: Some of the possible decay channels for a ^{78}Kr beam impinged on a ^{98}Mo target.

Each of the channels has a different probability to be produced, which is dependant on the beam energy. This probability is denoted by the *cross section* and its unit is the barn ($= 10^{-28}\mathrm{m}^2$). The larger the cross section for a specific reaction, the higher the quantity of that recoil mass is produced. Figure 3.3 shows an example of the different reaction channel cross sections, as a function of ion beam energy for the reaction studied here, as simulated by the program PACE4 [6].

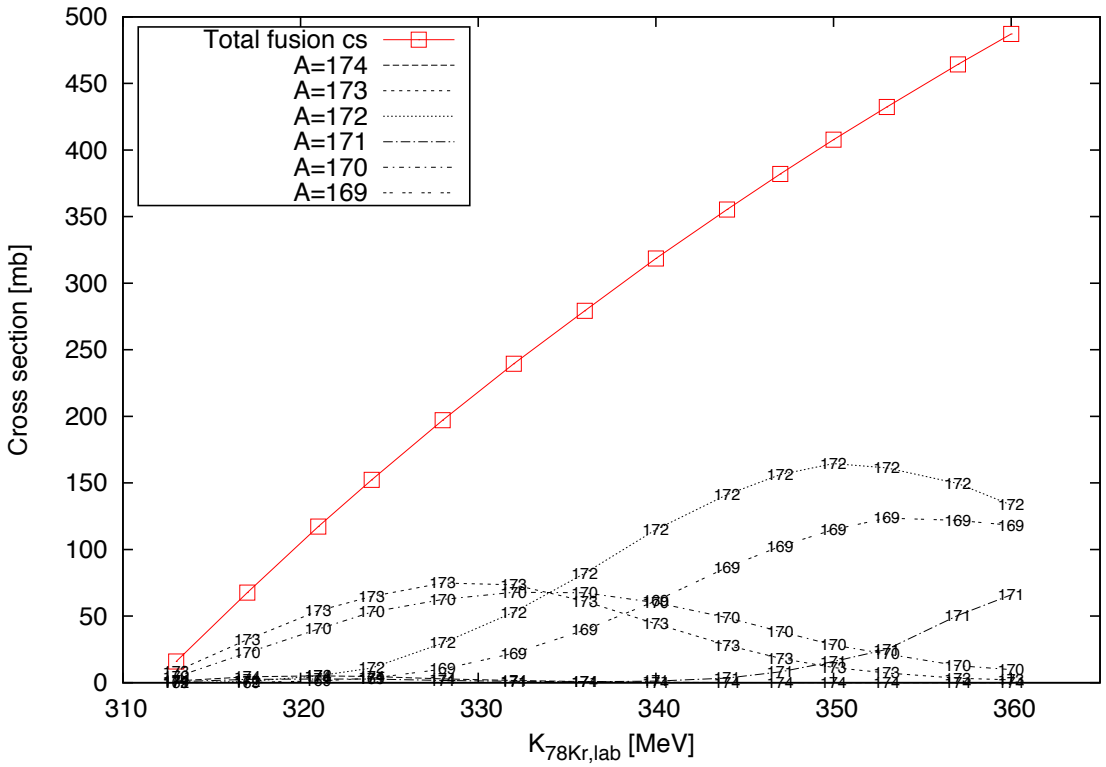

Figure 3.3: Cross section for different masses produced in the reaction of ^{78}Kr and ^{98}Mo as simulated by the program PACE4. The total cross section of all recoil products is highlighted in red. The energy of the beam is given as in the laboratory frame.

The general trend shows cross sections for particular masses increasing and then decreasing again. The decrease is due to the fact that it becomes energetically more favourable for more particles to be emitted as the beam energy increases.

Note that in this figure the separate cross sections for each mass include up to 6 possible isobars (i.e. the cross section for A=172 is the total probability for all possible isobars to be produced including, but not limited to: ^{172}Pt, ^{172}Ir, ^{172}Os, ^{172}Re and ^{172}W). The

contribution from each isobar is not equal. For example, at a beam energy of 350 MeV, the cross section for ^{172}Os is 107 mb, whereas for ^{172}Re it is 9.4 mb.

Figure 3.3 is based on data from an output file of a theoretical prediction given by the PACE4 program, for the specific reaction of ^{78}Kr and ^{98}Mo. It is referred to several times in the subsequent chapters and more details of how the predictions are made can be found in references [6] and [7].

3.2. Reaction kinematics

In order for the CN to be created, the projectile must be energetic enough. In this case an accelerator must be used to reach such energies. Ionisation of the projectile particles allows for greater acceleration of the beam, that is necessary to overcome the Coulomb barrier acting between the protons of the target and beam nuclei.

The first calculations proceed by finding the minimum energy necessary for the ion beam to overcome the Coulomb barrier. The Coulomb potential is approximated as the potential between a point charge and a homogeneously charged sphere, as derived from Gauss' law. The potential energy barrier, V_{C} is given by

$$V_{\mathrm{C}} = \frac{Z_{\mathrm{p}} Z_{\mathrm{t}}}{4\pi\varepsilon_0 R}. \tag{3.2}$$

Here, Z_{p} is the atomic number of the beam nuclei, Z_{t} the atomic number of the target nuclei and ε_0 is the permittivity of free space ($= 8.85 \times 10^{-13}\mathrm{Fm}^{-1}$). R is the distance between the two charge centres when the nuclei are in contact, or the distance which is needed to be overcome - approximately equal to the sum of the two radii:

$$R = r_0(A_{\mathrm{p}}{}^{\frac{1}{3}} + A_{\mathrm{t}}{}^{\frac{1}{3}}) \tag{3.3}$$

A_{p} and A_{t} are the the masses of the projectile and target nuclei, respectively. r_0 is a constant taken as 1.37 fm. The value of r_0 generally lies between 1.2 - 1.3 fm [8], [9], [10]. However, upon final calculations for the Coulomb barrier, in the case of ^{78}Kr and ^{98}Mo, these values give a clear underestimate. Thus, the value chosen here has been adopted

according to Bass [11], which in his paper suggests that r_0 should generally be adjusted, if necessary, by a fit to fusion and scattering data. This result comes from the general understanding that the value of the Coulomb barrier is not sharply defined.

The energy calculated as V_C, is that required in the centre of mass (CoM) reference frame. If the velocity of the CN, $\boldsymbol{v}_{\mathrm{cn}}$, is known, it is possible to compute the velocities of the beam and target in the laboratory frame by the use of Galilean transformations. Conservation of momentum can be applied to any collision in an isolated system. Here, the collision is treated as completely inelastic and conservation of momentum can be applied to obtain $\boldsymbol{v}_{\mathrm{cn}}$. The definition of a completely inelastic collision is that the two colliding particles stick together and move as one after collision:

$$m_{\mathrm{p}}\boldsymbol{v}_{\mathrm{p}} = (m_{\mathrm{p}} + m_{\mathrm{t}})\boldsymbol{v}_{\mathrm{cn}}, \tag{3.4}$$

where $m_{\mathrm{p}}\boldsymbol{v}_{\mathrm{p}}$ is the momentum of the projectile before the collision and $(m_{\mathrm{p}} + m_{\mathrm{t}})\boldsymbol{v}_{\mathrm{cn}}$ is the momentum of the CN after the collision. Rearranging gives

$$\boldsymbol{v}_{\mathrm{cn}} = \frac{m_{\mathrm{p}}\boldsymbol{v}_{\mathrm{p}}}{m_{\mathrm{p}} + m_{\mathrm{t}}}. \tag{3.5}$$

This is also the velocity in the centre of mass reference frame: $\boldsymbol{v}_{\mathrm{cn}} = \boldsymbol{v}_{\mathrm{com}}$. It follows from 3.5 that

$$E_{\mathrm{k,cn}} = \frac{m_{\mathrm{p}}}{m_{\mathrm{p}} + m_{\mathrm{t}}} E_{\mathrm{k,p}}. \tag{3.6}$$

Where $E_{\mathrm{k,cn}}$ and $E_{\mathrm{k,p}}$ are the kinetic energies of the CN and projectile, respectively.

To convert from the laboratory frame to the CoM frame velocity, $\boldsymbol{u}_{\mathrm{p}}$, all that is necessary is to subtract the velocity of the centre of mass from the laboratory velocity:

$$\boldsymbol{u}_{\mathrm{p}} = \boldsymbol{v}_{\mathrm{p}} - \boldsymbol{v}_{\mathrm{com}}, \tag{3.7}$$

for the projectile, and for the target nucleus:

$$\boldsymbol{u}_{\mathrm{t}} = 0 - \boldsymbol{v}_{\mathrm{com}}. \tag{3.8}$$

Now equation 3.5 can substitute in for $\boldsymbol{v}_{\mathrm{com}}$ into 3.7 to obtain

$$\boldsymbol{u}_{\mathrm{p}} = \frac{m_{\mathrm{t}}\boldsymbol{v}_{\mathrm{p}}}{m_{\mathrm{p}} + m_{\mathrm{t}}}. \tag{3.9}$$

Similarly the expression for $\boldsymbol{u}_{\mathrm{t}}$ yields

$$\boldsymbol{u}_{\mathrm{t}} = -\frac{m_{\mathrm{p}}\boldsymbol{v}_{\mathrm{p}}}{m_{\mathrm{p}} + m_{\mathrm{t}}}. \tag{3.10}$$

In terms of momentum, $\boldsymbol{p}_{\mathrm{com}}$ in the CoM reference frame is:

$$\boldsymbol{p}_{\mathrm{t,com}} = m_{\mathrm{p}}\boldsymbol{u}_{\mathrm{p}} = \frac{m_{\mathrm{p}}m_{\mathrm{t}}}{m_{\mathrm{p}} + m_{\mathrm{t}}} \cdot \boldsymbol{v}_{\mathrm{p}} = \mu\boldsymbol{v}_{\mathrm{p}} \tag{3.11}$$

and

$$\boldsymbol{p}_{\mathrm{p,com}} = m_t\boldsymbol{u}_{\mathrm{t}} = -\frac{m_{\mathrm{t}}m_{\mathrm{p}}}{m_{\mathrm{p}} + m_{\mathrm{t}}} \cdot \boldsymbol{v}_{\mathrm{p}} = -\mu\boldsymbol{v}_{\mathrm{p}}. \tag{3.12}$$

Here μ is the reduced mass, and the momenta $\boldsymbol{p}_{\mathrm{t,com}}$ and $\boldsymbol{p}_{\mathrm{p,com}}$, are of equal magnitude but opposite in direction. The total kinetic energy in the CoM frame, $E_{\mathrm{k,com}}$, is a sum of the kinetic energies of the projectile and target:

$$E_{\mathrm{k,com}} = E_{\mathrm{k,p,com}} + E_{\mathrm{k,t,com}}. \tag{3.13}$$

Finally, using equations 3.11 and 3.12, equation 3.13 can be re-written in terms of momentum and re-arranged to give:

$$\begin{aligned} E_{\mathrm{k,com}} &= \frac{\boldsymbol{p}_{\mathrm{p,com}}^2}{2m_{\mathrm{p}}} - \frac{\boldsymbol{p}_{\mathrm{p,com}}^2}{2m_{\mathrm{t}}} \\ &= \frac{m_{\mathrm{t}}}{m_{\mathrm{t}} + m_{\mathrm{p}}} E_{\mathrm{k,lab}}. \end{aligned} \tag{3.14}$$

The minimum amount of energy required to overcome the Coulomb barrier was V_{C}, as deduced in equation 3.2. If $V_{\mathrm{C}} = E_{\mathrm{k,com}}$, equation 3.14 can be re-arranged to determine the minimum amount of energy required in the laboratory frame that is necessary to achieve fusion. It is normally the case that experiments will run at higher energies than the Coulomb barrier, but this calculation provides the approximate minimum requirement of energy needed.

3.2.1 Excitation energy

The kinetic energy in the CoM system, is equivalent to the excitation energy of the compound nucleus. This is the amount of "extra" energy available to those particles that will evaporate. The excitation energy is given by:

$$E^* = Q + E_{\mathrm{k,com}}, \tag{3.15}$$

where Q is the *Q-value*. The Q-value is equal to the change in binding energies between the colliding nuclei and the compound system. In this case:

$$\begin{aligned} Q &= (m_{\mathrm{initial}} - m_{\mathrm{final}})c^2 \\ &= (m_{\mathrm{t}} + m_{\mathrm{p}} - m_{\mathrm{cn}})c^2. \end{aligned} \tag{3.16}$$

In general, for compound nuclei produced close to stability, it is most likely that neutrons are evaporated as they require less energy to do so. Other light particles such as protons and alpha particles are also evaporated but it is more difficult because they are required to overcome the Coulomb barrier as a result of their electric charge. However, for CN closer to the neutron deficient side of the nuclear chart, the separation energy for neutrons increases, whilst for protons it decreases, meaning charged particle emission will compete and dominate over neutron emission. Therefore, what type of particle emission will occur is dependent on where in the nuclear chart the CN is created.

3.3. Evaporated particle distribution

The evaporated particles can have a range of energies that is lower than the excitation energy of the nucleus, E^*, minus the separation energy, S_x, of the emitted particle x. The probability of emitting a particle x with a specific energy, below the maximum (leaving the CN in an excited state) is dependant on many parameters, including the inverse cross section for the reaction and level densities of the CN and recoil nuclei [7], [12].

The full mathematical treatment requires a statistical mechanical approach using the Fermi gas model to compute the level densities [13]. For emission of neutrons, the final energy spectrum has the form [14]:

$$N(\varepsilon)d\varepsilon = \frac{\varepsilon}{T^2}e^{-\frac{\varepsilon}{T}}d\varepsilon. \tag{3.17}$$

The function is a Maxwellian distribution with the most probable emission energy T, and the actual emission energy of ε.

Similarly, [14] also gives the distribution for charged particles as

$$N(\varepsilon)d\varepsilon = \frac{\varepsilon - \varepsilon_s}{T^2}e^{-\frac{\varepsilon-\varepsilon_s}{T}}d\varepsilon, \tag{3.18}$$

where ε_s is the threshold for charged particle emission (which is 0 for neutrons). Thus the maximum energy a charged particle can have is $E^* - S_\mathrm{x} - \varepsilon_\mathrm{s}$ [14], [13]. The distribution sits slightly higher in value than for neutrons because of the increased energy required to overcome the Coulomb barrier.

It has been described that particles are evaporated from the compound nucleus in analogy to molecules leaving the surface of a hot liquid [15]. Figure 3.4 shows the evaporation for light particles for the reaction of ^{78}Kr and ^{98}Mo at $E_\mathrm{k,lab} = 357$ MeV as simulated by the PACE4 program.

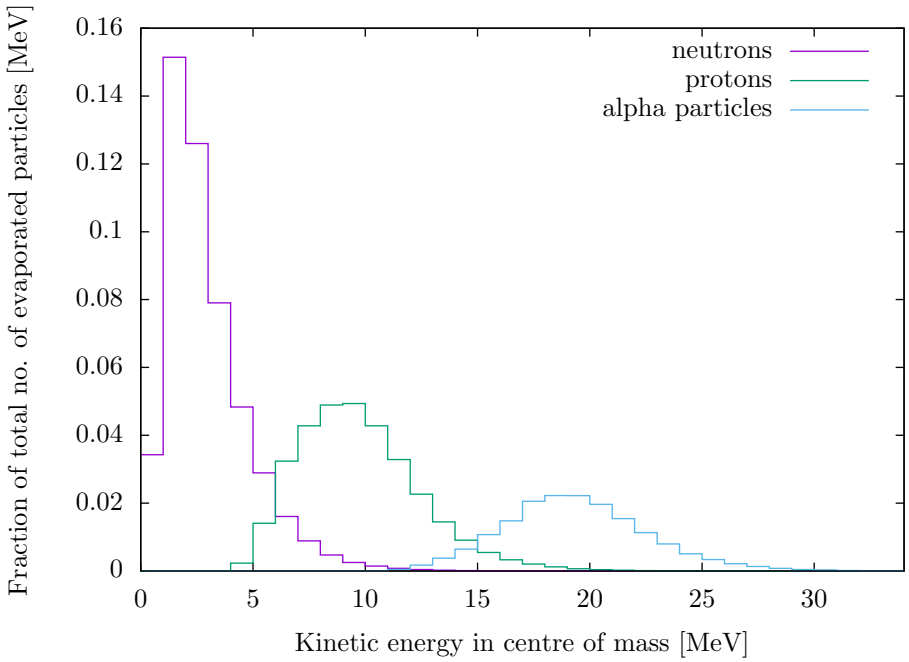

Figure 3.4: Energy distributions in CoM of evaporated particles after a ^{78}Kr on ^{98}Mo reaction at $E_{\mathrm{k,lab}} = 357$ MeV as simulated by PACE4

The average kinetic energies as taken in the CoM reference frame vary depending on the particle, and are ≈ 2 MeV for neutrons, 9 MeV for protons and 19 MeV for alpha particles, for this reaction.

3.4. Angular distribution and acceptance

Since the CN has essentially forgotten its mode of formation, there is no preferred direction for the decay products. It is expected that the neutron and proton evaporation distributions should be isotropic in the centre of mass frame. Therefore, in the laboratory frame more particles will appear to be emitted in the forward direction.

The recoiling nucleus, also has some small change in its direction as a result of the particle evaporation. The maximum change a recoil can have, is when the evaporated particle is emitted at 90° relative to its direction. This is also the *most probable* angle of emission. This is because, in spherical polar coordinates, the detector covers a larger area at 90° than it does at 0°, therefore counting more. This is more clear when looking at equation

3.19. The area, A, of the detector is given by [17]:

$$A = 2\pi r \int_{\theta_0}^{\theta_1} \sin(\theta) d\theta \tag{3.19}$$

where r is the distance to the detector, and θ_0 to θ_1 are the angles through which the detector covers with respect to the central axis of the system.

An approximation for the angular change of the recoil, θ_r, after the evaporation of one particle at 90°, is given by [16]:

$$\theta_\mathrm{r} \approx \frac{\boldsymbol{u}_\mathrm{r}}{\boldsymbol{v}_\mathrm{cn}} = \frac{m_\mathrm{cn}}{m_\mathrm{cn} - m_\mathrm{e}} \sqrt{\frac{m_\mathrm{e}}{m_\mathrm{p}}} \sqrt{\frac{E_\mathrm{k,e,com}}{E_\mathrm{k,p,lab}}}, \tag{3.20}$$

where $\boldsymbol{u}_\mathrm{r}$ is the velocity of the recoil, m_e is the mass of the evaporated particle and $E_\mathrm{k,e,com}$ is the kinetic energy of the evaporated particle in the CoM frame. Considering the reaction here, $E_\mathrm{k,p,lab} = 357\,\mathrm{MeV}$, the compound nucleus is ^{176}Pt and the CoM energies for n, p and α particles, are 2 MeV, 9 MeV and 19 MeV, respectively. Inserting those values into equation 3.20, θ_r can be determined as 0.006 rad for neutrons, 0.012 rad for protons and 0.356 rad for alpha particles. To clarify, for example, if the CN emits a proton at a 90° angle, then it will diverge from its original path by 0.012 radians. The values for the evaporated particle CoM energies are approximate and are calculated from the PACE4 program [6].

These calculations determine what recoils it is possible to transfer through MARA (and thus be detected at the focal plane). The parameter mostly influencing transmission of particles through the separator is the *solid angle acceptance* [18]. The number of recoils that are transferred to the focal plane from the target increases as the solid angle becomes larger. For MARA the angular acceptance is defined differently for the horizontal and vertical directions and has the values of 45 mrad and 55 mrad, respectively, or in total 9.9 msr [16]. Therefore it is clear that recoils involving alpha evaporation are less likely be detected since they are outside of MARA's acceptance. It is still possible however, that some recoils can be detected from alpha evaporation channels, since not all alpha particles will evaporate at 90°. It is only less probable they will be detected.

Finally, it should also be noted that it is not completely accurate to quote a single

number for the transmission of a recoil mass spectrometer. The transmission is dependant on reaction kinematics, reaction channel and target thickness for any individual experiment. Therefore the numbers above give only an indication of the value.

3.4.1 Aside on barriers

Apart from overcoming the Coulomb barrier, the complete force felt by the projectile is affected also by the nuclear and centrifugal forces (angular momentum). The Coulomb potential was described in the previous section in equation 3.2. The nuclear potential, as a function of distance r from the nucleus centre, can take many forms, but frequently is described by the Woods-Saxon potential [19]:

$$V_{\mathrm{N}}(r) = \frac{V_0}{1 + e^{\frac{r-R}{a}}}. \tag{3.21}$$

R is given by equation 3.3, V_0 denotes the depth of the potential well and a represents the "surface thickness" of the nucleus. The centrifugal barrier is given by [19]

$$V_{\mathrm{cent}}(r) = \frac{\hbar}{2\mu}\frac{l(l+1)}{r^2}, \tag{3.22}$$

where μ is the reduced mass and l is the orbital angular momentum quantum number of the incident particle. The total potential is then:

$$V_{\mathrm{tot}} = V_{\mathrm{C}} + V_{\mathrm{N}} + V_{\mathrm{cent}}. \tag{3.23}$$

The actual *interaction barrier* is the value of V_{tot}, at the point in which the colliding nuclei touch. For very high values of angular momentum, the total potential is negative and the nuclei do not quite fuse. At this point, the fission process will dominate and the CN is not properly formed. This is because the height of the fission barrier is inversely proportional to the angular momentum number [20]. If fusion evaporation reactions are desired to produce high spin states for an experiment, one must also think about the consequence of when fission will dominate.

It is worth noting, that it is the interaction barrier that inhibits neutrons with large

amounts of angular momentum from escaping. The evaporated neutrons are therefore mostly in $l = 0$ or 1 states. Thus through neutron evaporation, the CN loses most of its excitation energy, but only a little of its angular momentum, resulting in high spin states of the remaining nucleus.

4. Target interactions

4.1. Charge state distribution

Any ion traversing through a target material, will change its electronic charge when colliding with other atoms. This is due to the exchange of electrons between the ion and target atoms. The recoil produced after a fusion evaporation reaction is therefore also subject to these charge exchange collisions. In any one collision with a target atom, the recoil atom can become excited. The time between two such collisions is much shorter than the time it takes for atomic de-excitation; meaning that the excited electron does not have time to decay to its ground state before the second collision [21]. This reduces the electron capture cross section and as such the average charge for heavy ions in solid target materials can become quite high.

Theoretical calculations for this average charge state are exceptionally complicated since both ion and target atoms are many-body systems. Detailed knowledge on the cross sections for electron capture and electron loss are required. Furthermore, possible multiple electron transfer in single collisions make a simplified equation impossible.

Empirical methods are mostly adopted to estimate such charge states for comparison with experimental observations. One such formula is that described by Nikolaev [22] in which the average charge state, $\bar{q}$, is given by

$$\bar{q} = Z\left(1 + \left(\frac{v}{Z^{\alpha} v_{\cdot}}\right)^{-\frac{1}{k}}\right)^{-k}, \tag{4.1}$$

where $v_{\cdot} = 3.6 \times 10^{6}\mathrm{m/s}(= 0.012\mathrm{c})$, $k = 0.6$ and $\alpha = 0.45$. Z and v are the atomic number and velocity, respectively, of the recoil in this case, but the formula can also be used to calculate $\bar{q}$ of the unreacted beam particles after the target. This formula is specifically adopted for carbon as a target media.

More recent formula have been developed, for example, by Schiwietz and Grande [21],

that determine the average charge state for different target medium. Most of those newly developed formula give values close to that first developed by Nikolaev, but are more complex to utilize. If a carbon foil is placed after the target, it allows us to adopt equation 4.1, making calculations more simplified. Thus, it was the decision for this commissioning run to place a Carbon foil after the ^{98}Mo target. In addition, the Carbon foil is equally as important for the re-setting of abnormally high charge states as a result of Auger electrons following the potential CN de-excitation via internal conversion.

It is necessary to point out that the initial charge state of the ion beam does not influence the final charge state of the recoil. This is due the the high number of collisions the recoil has in the target before exiting; meaning that it reaches some equilibrium charge state that is dependant only on the recoil velocity and its atomic number.

For a complete understanding, it is also necessary to consider the distribution of states around the average. The distribution is a consequence of competition of electron capture and losses in the target. The width of the distribution ($d_{\bar{q}}$), also given in [22] is:

$$d_{\bar{q}} = d_0\sqrt{\bar{q}\left[1-\left(\frac{\bar{q}}{Z}\right)^{\frac{1}{k}}\right]}, \tag{4.2}$$

with $d_0 = 0.5$, and the distribution is assumed to be Gaussian. It is noted in [22] that deviations from $\bar{q}$ and $\mathrm{d}_{\bar{q}}$ when compared with experimental values arise from the shell structure of the recoil ions. $\mathrm{d}_{\bar{q}}$ is a minimum for those ions whose shells are completely filled. Deviations for $\bar{q}$ of no more than 5% for ions greater than Z = 20, and for $d \approx 20\%$ are to be expected [22].

4.2. Energy loss

Any ion traversing through some target medium, interacts simultaneously with many of the target electrons and will feel an impact from the attractive Coulomb force [23]. Depending on the proximity of the ion, the impact may be enough to raise an electron to a higher orbital shell, or completely remove it from the atom [23]. The energy given to the electron

is at the cost of the projectile energy. The ions can also interact with the target nuclei, but the energy loss is almost insignificant (for beam energies of MeV) when compared with the loss from electron interactions. This energy loss of an ion from a target interaction is called the *stopping power*. The loss in energy of the ion is given by:

$$\Delta E = \frac{dE}{dx}t, \tag{4.3}$$

where ΔE is the loss in ion energy and t is the target thickness. $\frac{dE}{dx}$ is the stopping power for a specific ion in the target at a particular energy. Equation 4.3 is valid only for thin targets, which is the case for this experiment. This means the energy loss is small enough that the stopping power is almost the same for the initial beam as for the reduced beam energy after traversing the medium. For thick targets, where the beam would be drastically reduced in intensity, one would also have to consider broadening of the final *straggling* value due to the non-linearity of stopping powers [25]. Straggling is the variation in energy loss of an ion traversing some medium. The stopping power of any ion-target combination can be calculated using the program SRIM. SRIM uses experimental data and empirical scaling to arrive at values for the stopping power. Details of these calculations can be found in reference [25].

For this experiment, there are two important cases to consider: the energy loss from the ^{78}Kr projectile interacting with the target before the CN is formed and the energy loss as the recoil traverses the remainder of the target. The velocity of the recoil is naturally lower than the projectiles and the atomic number is higher, therefore it is expected that the energy loss from the recoil in the target is higher than for the incoming ^{78}Kr particles. A sketch is illustrated in figure 4.1 to clarify.

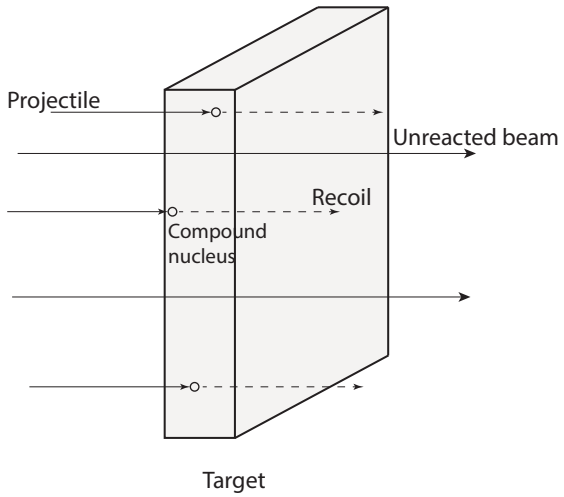

Figure 4.1: Schematic showing that the target is some finite thickness, which both the projectile and recoil nucleus must traverse through. Different locations of the CN composition depict how much kinetic energy the final recoil has after the target.

It is clear that those CN created deeper in the target i.e. close to exiting the medium, will have different kinetic energies than those created near the front surface. This gives some variation in the final kinetic energy of the recoil as it exits the target. As equation 4.1 states, the average charge state of a recoil is dependent on its velocity, thus there is going to be some *distribution* about the average charge state of the recoil. It is necessary to point out here, that relatively few CN are made when compared to the amount of projectiles hitting the target. A large proportion of the beam will not react with the target at all, instead passing directly through it. The unreacted beam is therefore mixed with the recoils immediately after the target.

Another source of energy variation that may need to be considered is in the beam itself when accelerated in the cyclotron. Although the beam from the cyclotron should be monoenergetic, this is not completely true and standard practice assumes the energy spread to be about $\pm 1\%$ [24] of the beam energy. The total energy variation of the recoils is then a contribution of the beam loss in the target, the recoil loss in the target and the broadening from the beam not being completely mono-energetic.

Finally, there is a small amount of energy loss due to the particle evaporation processes. Since the evaporation of multiple light particles is considered to be isotropic there is an equal momentum kick to the recoil in all directions from several evaporations. Therefore, the velocity of the recoil stays approximately constant whilst the mass decreases. The kinetic energy of the recoil then also decreases resulting in some energy loss. This value is essentially negligible, contributing to only a small reduction in the kinetic energy of the final recoil in the laboratory frame; when compared to the loss from projectile-target and recoil-target interactions. Therefore, it is not taken into consideration in the results of this thesis.

5. Instrumentation - MARA

5.1. Main components and mathematics

MARA is a vacuum-mode recoil mass separator designed specifically to separate beam and fusion recoil products from one another, with the additional benefit of mass separation of those recoils. Recoil separators such as MARA, are required specifically for symmetric or inverse kinematic reactions. In normal kinematic reactions, where the beam is lighter than the target nucleus, gas-filled separators are used to separate beam from recoil products. With gas-filled separators, it is difficult to separate the unreacted beam from recoils when experimenting in the lighter mass region ($\approx {}^{100}$Sn and below) [16], thus for these types of experiments vacuum-mode separators are used. Here a symmetric reaction is such that the projectile is approximately equal in mass to the target nuclei, which is the case for the reaction being analysed here. In inverse kinematics, the projectile is much heavier than the target nuclei. Separation is performed through the use of magnetic and electric components.

In its most basic form, MARA consists of a quadrupole triplet, an electrostatic deflector, a magnetic dipole and detectors at the focal plane. The target chamber is shown in the left of figure 5.1, which is where the ^{98}Mo target is positioned. After the reaction, the recoils and the unreacted beam particles first pass through the quadrupole triplet, which focuses diverging products. The first and third quadrupoles focus in the horizontal plane (and defocus vertically). The second quadrupole focuses in the vertical plane (and defocuses horizontally). The result is point to parallel focusing of the particles as they pass through the triplet. The basic design of MARA can be seen in figure 5.1 [16].

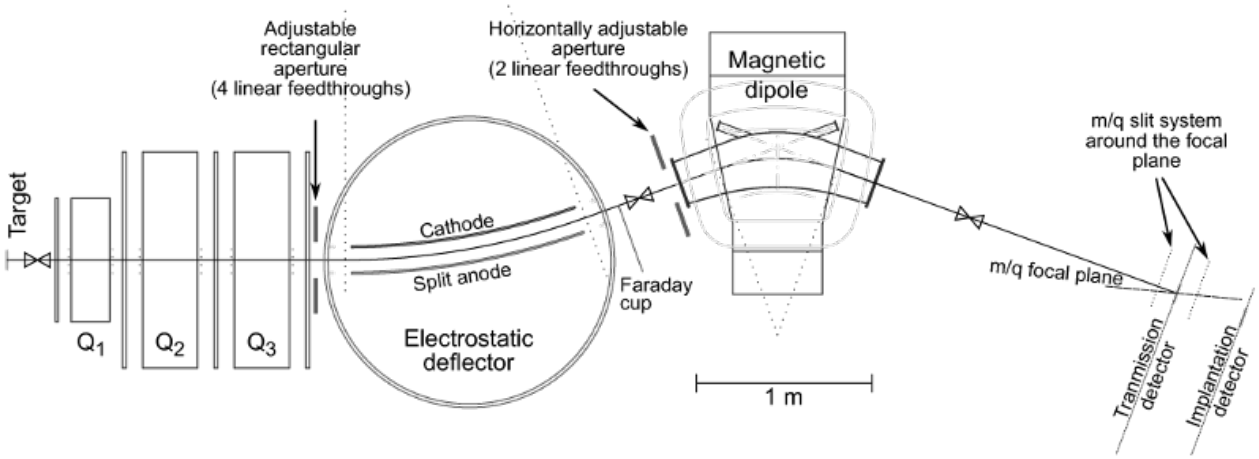

Figure 5.1: Layout of MARA. The optical element on the left, consisting of Q_1, Q_2 and Q_3 is the quadrupole triplet. Recoils are bent according to the electrostatic deflector and magnetic dipoles. They are brought to focus at the transmission detector in the focal plane.

After the triplet, particles enter an electrostatic deflector followed by a magnetic dipole. These components, including the quadrupoles, function through the use of Lorenz's formula, which describes the force on a charged particle as it moves through an electromagnetic field:

$$\boldsymbol{F} = q(\boldsymbol{E} + \boldsymbol{v} \times \boldsymbol{B}). \tag{5.1}$$

Here, q is the particle charge, $\boldsymbol{v}$ is its velocity, $\boldsymbol{E}$ the electric field and $\boldsymbol{B}$ is the magnetic field. Considering only the second component of the system, the electrostatic deflector, equation 5.1 can be written in terms of the electric field component. The magnitude of F is then

$$F = ma = qE, \tag{5.2}$$

where a is the centripetal acceleration: $a = v^2/\rho$, and m is the particle's mass. Thus a charged particle when placed in an electric field, will move in circular motion, of radius ρ, as long as the field is parallel to the particles trajectory. Substituting into equation 5.2, for

the centripetal acceleration, defines a parameter called the *electric rigidity*, χ_E as

$$\chi_E = \frac{v^2 m}{q} = E\rho. \tag{5.3}$$

The electric rigidity describes how easily the trajectory of a charged particle is bent under an electric field. The radius of curvature, ρ, is set by the bending radius of the anode and cathode inside the deflector (see table 5.1). The result is the deflector bends particles according to their kinetic energy per charge. The aim is to set the electric field of the deflector such that a specific recoil of known $\frac{E_\mathrm{k}}{q}$ runs along the deflectors central or *optical* axis. χ_E is usually very different for recoil particles and unreacted beam, therefore it is fairly easy to remove the unreacted beam in this way.

The third major component is the magnetic dipole, which bends the remaining recoils by mass per charge. Analogously to an electric field, the magnitude of the force on a particle in a magnetic field can be written:

$$F = ma = qvB. \tag{5.4}$$

As long as the velocity component, v, is perpendicular to the field, the particle will move also in a circular orbit, of radius ρ. This is still the bending radius, but this time it is set by the magnetic dipole, whose value can be found in table 5.1. Again substituting in for the centripetal acceleration one can define the *magnetic rigidity*, χ_B as

$$\chi_B = \frac{vm}{q} = B\rho. \tag{5.5}$$

The magnetic rigidity then defines how easily a particles trajectory can be bent in a magnetic field. This time particles with different momentum/charge ratio will follow different paths through the field. As such, the magnetic field for a particle of known momentum and charge can be made to travel along the central axis of the dipole.

For an electric field the extra component of velocity in the definition of rigidity, relative to the magnetic rigidity, means that the particles are bent according to their kinetic energy

and not their momentum as for magnetic fields. This is an important distinction. Since the deflector separates according to energy per charge, the second role of the dipole is to cancel the energy dispersion in the focal plane caused by the deflector.

The supplied voltage for the electrostatic deflector can be calculated by applying Gauss' law ($\oint \boldsymbol{E} \cdot d\boldsymbol{A} = Q/\epsilon_0$) to the two cylindrical electrodes that are infinitely long. The electric field is calculated at equidistance between the two electrodes. The electric field is related to the voltage via:

$$d\boldsymbol{V} = -\boldsymbol{E} \cdot dr \tag{5.6}$$

After integrating both sides and taking the radius of curvature to be the central point between the two electrodes ($r = \rho = \frac{1}{2}(R_1 + R_2)$), V is given in terms of the electric rigidity as

$$V(\chi_E) = \frac{1}{2}\ln\frac{R_1}{R_2}\chi_E. \tag{5.7}$$

R_1 and R_2 are correspondingly the radii of the inner and outer electrodes of the deflector, whose values are fixed.

The electric and magnetic fields focus the charged particles such that there is a fixed energy focus point at the end of the system, inside the focal plane. The focus is more specifically designed to coincide with a gas detector located at the focal plane, see section 5.2.1 for further details. As an analogy, one can think of the electrostatic components focusing the recoils in a similar manner to how light rays are focused through lenses in optical microscopy.

The parameters below are taken from [16] and describe some of the properties that were necessary for this study. The acceptance has already been described in section 3.4. The radii of the magnetic and electric dipoles are given, as well as the mass dispersion. The latter is explained in some detail in section 6.1.

Parameter	Value
Horizontal acceptance	45mrad
Vertical acceptance	55mrad
Radius (MD) ρ_M	1.00m
Radius (ED) ρ_E	4.00m
Mass Dispersion	8.1mm/%

Table 5.1: Optical properties of MARA

5.2. Focal plane

5.2.1 Detectors

The MWPC (Multi-Wired Proportional Counter) is a transmission detector used namely for time of flight measurements. It consists of three arrays of wires spaced 2 mm apart and 20 μm thick. The two outside arrays are held to ground (cathode) and the central array is held at high voltage (anode). The chamber is filled with a gas, which in this case isobutane. A particle that passes through the chamber ionises the gas atoms. Electron - ion pairs are created and electrons are accelerated by the electric field around the wires. The acceleration causes further electron - ion pairs being created in an avalanche effect. The result is an amplified charge proportional to the ionising effect of the initial incident particle. The position of where the particle has hit the wire is determined by the time it takes for the charge to traverse to opposite ends of the wire. The mass/charge focus for the MARA system is positioned at the MWPC detector.

The DSSD (Double-sided Silicon Strip Detector) is an implantation detector used for collecting data on particle position and energy. It is made of a semiconductor material with an intrinsic region sensitive to incoming particles. The DSSD utilised for this experiment, comprises of an arrangement of 48x128 strips (1mm x 1mm) resulting in a total of 6144 pixels. In this way, each pixel acts as a separate detector. In the intrinsic region, electron-hole pairs are created as the incident ion causes electrons to be transferred from the valence band to the conduction band of the semiconductor. The number of electrons transferred is

proportional to the energy of the incoming ion. Under the influence of an electric field, the electrons in the conduction band travel to an electrode, which can be measured as a pulse in outside circuitry. For each event occurring in the DSSD, the time, energy and position are recorded. The event type can not only be a recoil, but also a decay particle of a recoil (identifiable when used in collaboration with the MWPC).

5.2.2 Mass focal plane

An important feature of the MARA focal plane is that the focus of the masses, i.e the *mass focal plane*, is not quite perpendicular to the optical axis, and instead lies at some angle to it, as clarified in figure 5.2.

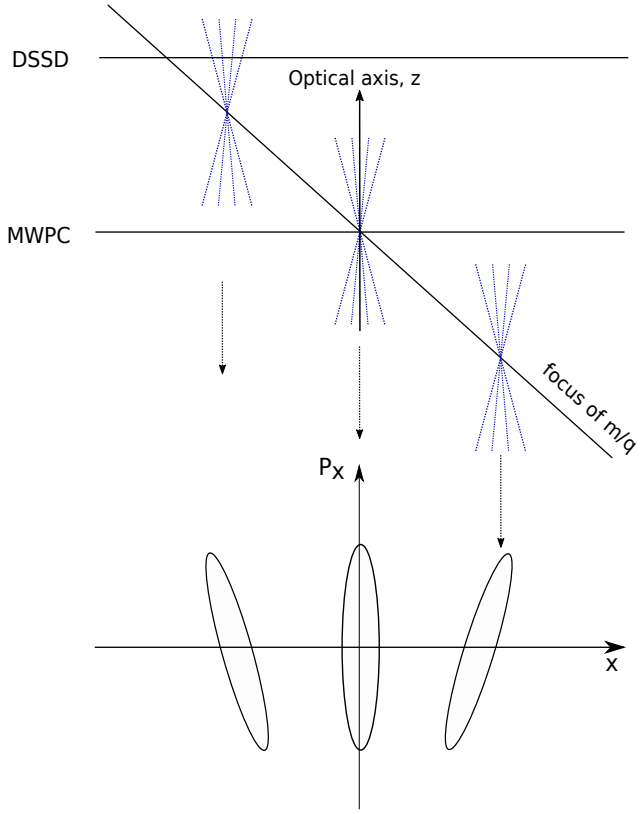

Figure 5.2: Schematic showing the tilted mass focal plane, and how the particles would look in phase space. Only the reference particle will deposit its energy centrally on the MWPC detector.

The *reference* particle is defined to be the recoil, which will reach the focal point completely centrally and is said to travel along the *optical axis* of the system. Different masses to the reference mass will be focused just before, or just after the MWPC. This tilted focal plane is a result of aberration effects arising from the focusing elements and is difficult to avoid. Figure 5.2 also shows how the recoils look in the corresponding *phase space* as seen at the MWPC. Phase space is a plot of the particles momentum vs. position and it is given in the diagram in only the x direction. The reference particle, which centrally passes through the MWPC has a corresponding ellipse lying perfectly upright in the phase space diagram. Those that are focused just before or after the MWPC have an angle to the P_{x} axis because their focussing is earlier or later in time.

6. Data acquisition and analysis

The data analysis in this experiment was completed using Grain software [26]. Grain analyses the raw data stream which is run via a sorting code to extract relevant information. The code is implemented in the programming language Java and can be altered, if required by the experimentalist. Data is visually displayed in a series of histograms. The interface looks as that shown in figure 6.1 and a list of histograms is displayed in the side panel on the left of the figure.

After the initial sort, a histogram of energy deposited [MeV] in the DSSD vs. time of flight (ToF) [ns] shows how the recoil products are separated from other particles entering the focal plane. The ToF axis is decreasing, left to right, in scale. A typical example of the type of plot produced can be seen in figure 6.1.

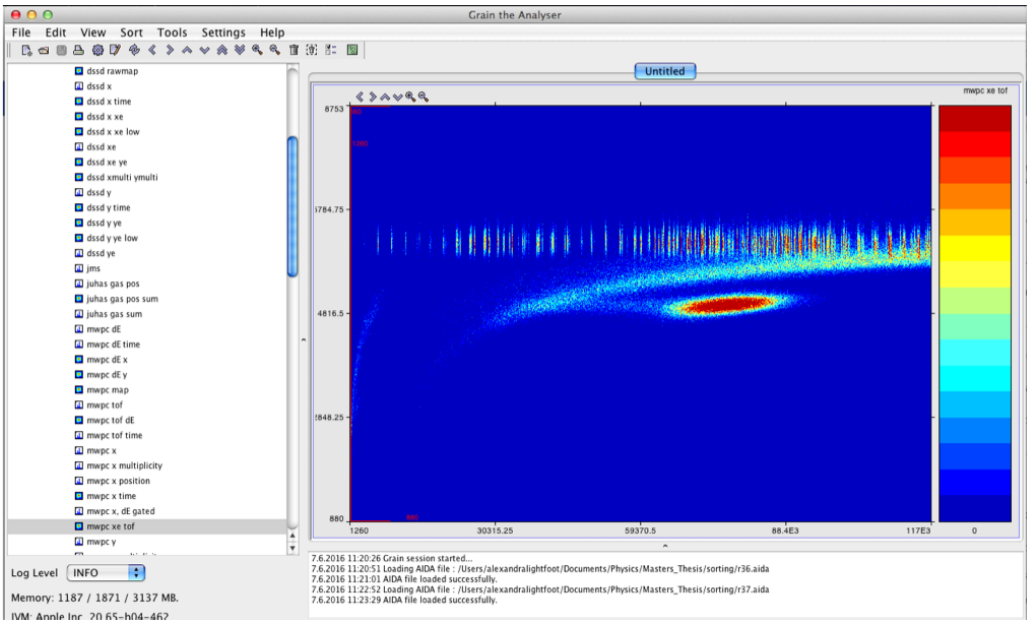

Figure 6.1: User interface for Grain and histogram of Energy [MeV] vs. ToF[ns], for all recoils entering the focal plane. The colour scale in the right of the image signifies the amount of recoils - going from blue, indicating no recoils, to red.

The time of flight is calculated by how long it takes for a particle to travel between

two detectors. In this case these detectors are the MWPC and DSSD located in MARA's focal plane, with known separation. The velocity of the recoils is determined by the target processes as described in section 4.2.

The scale in the right of the figure shows where there are no events detected, in the dark blue regions, to many events in the red regions. From figure 6.1 the recoils of interest are accumulated in the red region of the graph. The banana shaped buildup above this are scattered beam particles. The somewhat regular line bands above the beam scatter are artificial and come from scattered beam whose energy is over the maximum range of the ADC (Analogue to Digital Converter). Finally, the small banana shape spectrum in the leftmost centre of the figure, is most probably protons or alpha particles from the target which have been scattered into the acceptance of MARA.

To separate the recoils of interest from the scattered beam events, a gate can be set around them as shown in figure 6.2. A *code* has been designed to recognise the saved gate file and sort only that data in the selected area.

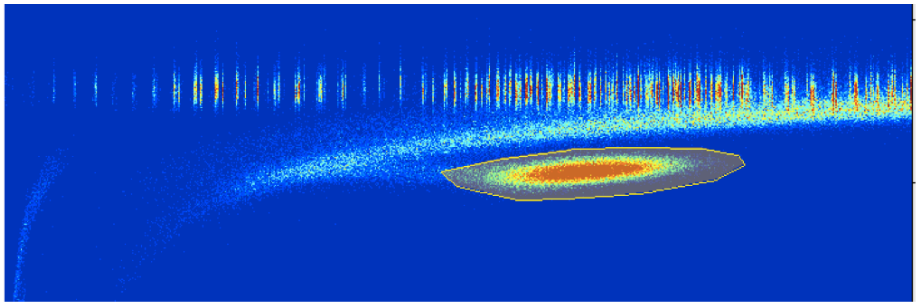

Figure 6.2: Zoomed in shot of Energy [MeV] vs. ToF [ns] histogram, giving an example of how gating is set on the recoil particles (highlighted in yellow)

Sorting produces a new histogram of an *approximate* phase space of the particles, as described in the end of the previous chapter 5.2.2. A typical histogram looks as that shown in figure 6.3. The approximation is made from building a histogram of angle, θ, vs. position instead of momentum vs. position. The angle that the x-component of velocity, v_x, makes with the z-component (optical axis) is so small that we can say that $\theta \propto v_x$ is a valid approximation. Since the formula for momentum is $P_x = mv_x$, then $v_x \propto P_x$, and thus $\theta \propto P_x$.

The new sorted data contains no unwanted events from, for example, scattered beam and the number of counts for each charge state of the recoils can therefore be determined. The axis in figure 6.3 are the change in position Δx [mm], analogous to θ, between the MWPC to the DSSD vs. position [mm] of where the recoil landed in the MWPC.

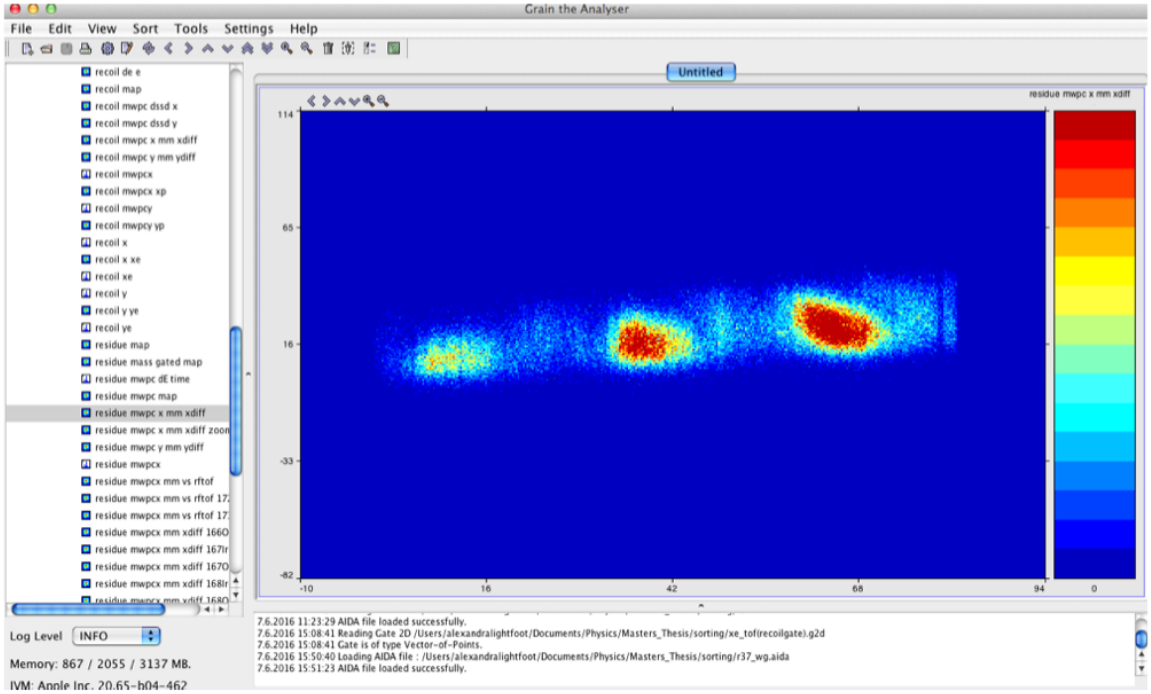

Figure 6.3: Recoils separated by charge after a sorting code is applied to a saved gate file

The code itself works such that the phase space histogram fills a pixel under the condition that there is a pixel i.e. signal in the MWPC histogram, and a pixel i.e. energy deposited in the DSSD histogram, within a certain time frame.

Three approximately circular distributions are produced, with each distribution indicating a different charge state. It is important to note that although the electric and magnetic fields have been set to focus only one specific recoil of interest at any one given time, the final phase space histogram can contain other overlapping distributions of recoils whose values of χ_{E} and χ_{B} are similar to that of the nuclei of interest. This is the case in figure 6.3, where it is clear that two masses are being collected. Additionally, the distribution between the more intense circles, is possibly an α evaporation channel, which can be deduced with the help of figure 3.3. The third charge state in the phase space diagrams lies too far away

from the reference and wouldn't provide accurate data for the number of counts, thus it wasn't considered.

6.1. Identification of charge states and masses

To identify exactly which charge states are shown it is easy to assume that the higher charge states have a lower χ_B value and thus bend more under the magnetic field. This would then correspond to the left most charge state in figure 6.3. For completeness, one can also use the equations regarding the optics of the charged particles to identify the charges and calculate where, with respect to the reference, they would be in the focal plane.

As stated in [16], the deviation from the optical axis of the mass of a charged particle from that of the reference particle is δ_m. The relation is given by

$$\frac{m}{q} = \frac{m_0}{q_0}(1 + \delta_m), \tag{6.1}$$

where m_0 and m are the masses of the reference and the detected recoil of interest, respectively. Similarly, q_0 and q are the charge states of the reference and the detected charge of interest. δ_m is the coordinate describing the relative difference in the m/q ratio, from that of the reference particle. This equation can be used along with equation 6.1 to calculate the location of the particle in the MWPC with respect to the location of the reference particle. Equation 6.2 describes how the shift in the particle position is related to δ_m:

$$\Delta x = (x|\delta_m)\delta_m, \tag{6.2}$$

where $(x|\delta_m)$ is the dispersion. This corresponds to the transfer coefficient that describes how deviation from the mass of the reference particle, effects the final position of the recoil in the MWPC. Δx is the physical distance in the MWPC that the recoil of interest lies from where the reference particle is positioned. By assuming, for example that $m_0 = m$, i.e. that there is only one mass coming to the focal plane of different charge states, equation 6.1 can be re-arranged to find δ_m and Δx can be determined.

$(x|\delta_m)$ has been previously calculated, also in [16] and has a value of 8.1 mm/%. This

means for each 1% deviation in mass (per charge) from the reference particle, the position changes by 8.1 mm.

For this method, Δx gives the separation between charge states in the focal plane. Separation between masses can also be determined, by similarly assuming that $q_0 = q$ to give a δ_m value, which corresponds to a change in mass by one unit for particles of the same charge.

6.1.1 Reference charge

The selected charge state for the first run was set to be 32.5. This was the chosen charge state for preliminary testing and this decision is based on equation 4.1. Whilst the average charge state can take any value, physically, only distributions of integer values will accumulate in the focal plane, as shown in figure 6.4, and equivalently 6.3:

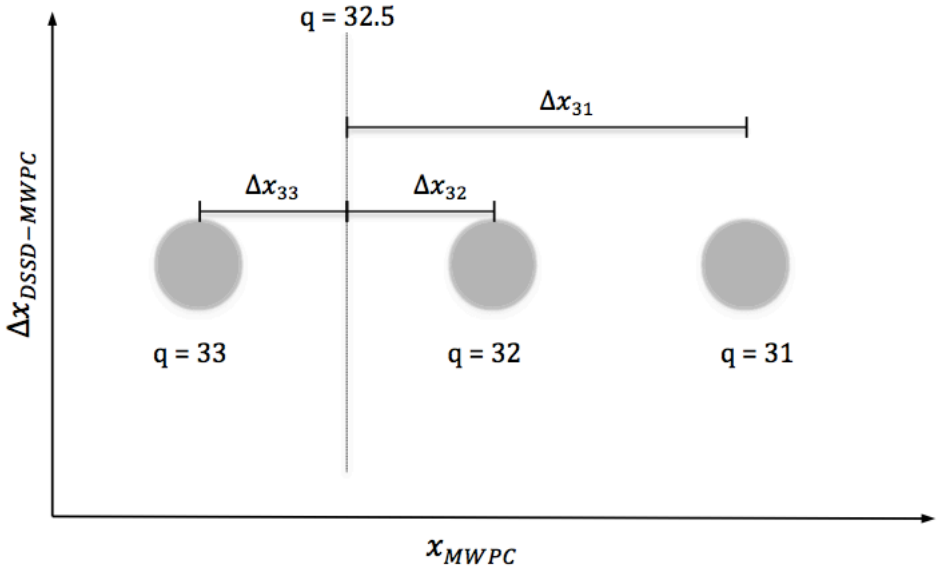

Figure 6.4: Sketch similar to that shown in figure 6.3 with labelled charge distributions and how they are shifted with respect to the reference charge. It is also shown how the distance Δx_q was defined.

The figure shows an example of labeled charge states and how Δx_q is defined. The values of Δx_q with respect to distance from the reference charge, for the first run (q = 32.5) have been calculated, using equations 6.1 and 6.2 and are presented in table 6.2:

Charge state[e]	Δx_q[mm]
33	-12.27
32	12.66
31	39.19

Table 6.1: Calculated distance of charge states from $q_0 = 32.5$ as seen in the MWPC

This table shows that for a change of one charge unit, the separation in the focal plane would be 24.93 mm. This is true for the reference charge of 32.5 with particles of the same mass. Charge states from $q = 29.5 - 32.5$ were scanned over, and for each data set the values of Δx_q were calculated. It is unnecessary to show all tables here, where the intention is only to explain how the charge states can be identified using optical equations.

6.1.2 Reference mass, parameter settings and calculations

If instead the charge is kept constant whilst only the mass changes by one unit, the result given by equation 6.1 is the separation in the focal plane between different masses for the same charge. For this experiment, the reference particle mass was set consistently for A = 173. The Reason for this specific selection is explained in more detail in section 8. It is useful to know, where mass 172 would appear in the focal plane, with respect to mass 173. If a charge state of q = 32.5 is assumed, whilst m_0 is taken to be 173 and m is 172, then $\Delta x_{mass} = 4.62$ mm. This means that masses 172 and 173 lie 4.62 mm away from each other at the focal plane. As such, it is possible that the distributions can overlap with one another and indeed this was found to be the case as is seen in figure 6.3. Noticable overlapping distributions will only appear if χ_E and χ_B are similar to that of the reference particle *and* the production cross section of that particular channel is high.

The numerical values in table 6.3 have been calculated using the formula in section 3.2 and are presented to provide an idea of the typical orders of magnitude that some of the values take. All calculations have been made using the following parameters:

	Element	Atomic mass	Atomic Number
Projectile	^{78}Kr	78	36
Target	^{98}Mo	98	42
Compound	^{176}Pt	176	78
Reference	^{173}Os	173	76

Table 6.2: Atomic mass and atomic number of reaction, compound and reference elements

Parameters values at Coulomb barrier (178 MeV in CoM):

	Projectile	Compound
E_{k} (Lab)[MeV]	320.46	142.43
Velocity[m/s]	2.82×10^7	1.25×10^7
Charge [e]	28.50	32.50
χ_E[MV]	22.5	8.7
χ_B[Tm]	0.799	0.701

Parameter values at a beam energy of 357 MeV :

	Projectile	Compound	Reference
E_{k} (Lab)[MeV]	357	158	150
Velocity[m/s]	2.97×10^7	1.32×10^7	1.29×10^7
Charge [e]	29.0	33.5	32.5
χ_E[MV]	24.6	9.4	9.2
χ_B[Tm]	0.829	0.710	0.714

Table 6.3: Parameter values at the Coulomb barrier and at 357 MeV beam energy

The result of equation 4.1 gave an average charge state of 32.5 for the compound nucleus with a kinetic energy of ≈158 MeV. Assumptions were made, that the reference particle would have a similar charge state and it was approximated to have a kinetic energy of 150 MeV. These numbers were used to determine the magnetic and electric rigidities for the MARA system, whose values are defined in table 6.3 for the first run. The rigidities naturally must be altered with the reference charge, thus the values of χ_B and χ_E are amended as the reference charge changes for each run.

7. Results

7.1. Calculation of energy losses

The depth at which the CN is formed determines how much energy the recoil has upon exiting the target. Calculations from SRIM give the stopping power of ^{78}Kr in ^{98}Mo as 2.40 KeV/($\mu g/cm^2$) for a beam energy of 357 MeV [25]. The target area density was 500 $\mu g/cm^2$. The thickness, t, of the target can easily be obtained in μm through the relationship: $t = \rho_A/\rho_V$, where ρ_A is the area density and ρ_V is the volume density. ρ_V was taken as 10.49 g/cm^2 [27], thus giving a thickness of 0.0476 μm. Using these values and by making use of equation 4.2, the energy loss of the beam in the first 10% of the target was calculated to be 1.19 MeV, whilst that in the last 90% of the target is 10.74 MeV. Thus the energy of the projectile is expected to vary between 356 MeV and 346 MeV as it traverses the target.

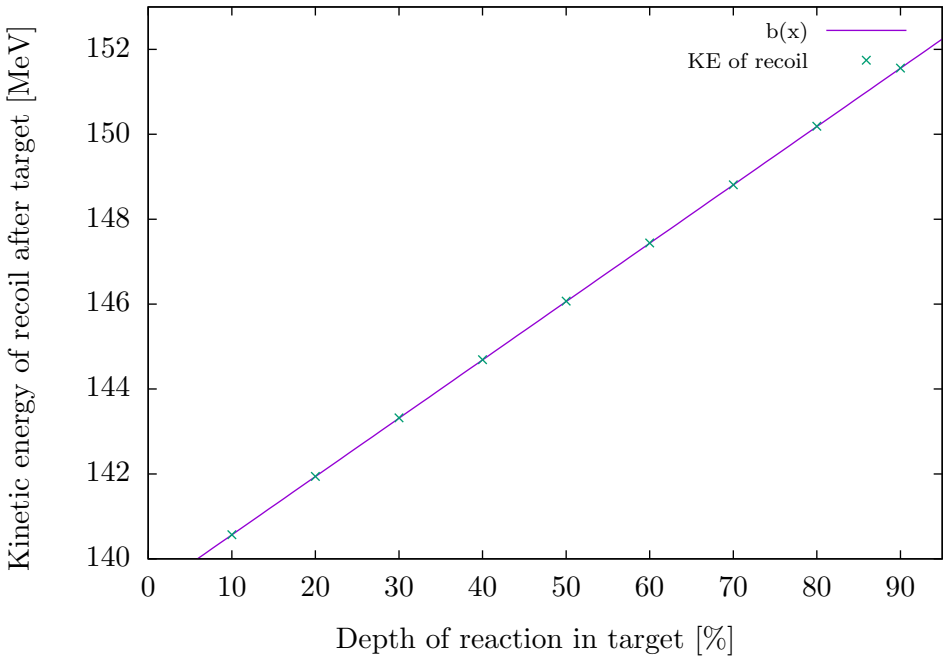

Figure 7.1: Plot to show how the energy of the recoil on exiting the target, is dependant on the depth in the target at which it was created.

To this value, we need to add the energy loss from the recoil as it traverses through the remainder of the target thickness. Again, SRIM gives the stopping power for ^{173}Os in ^{98}Mo as 3.80 KeV/($\mu g/cm^2$) for a recoil energy of 150 MeV [25]. Noticeably, the stopping of a recoil in the target contributes a larger portion of the total energy loss. Figure 7.1 shows the final energy of the recoil as it leaves the target, after both contributions to the losses have been subtracted.

It is appropriate to consider that the compound nuclei are approximately formed in the centre of the target. For this case, there is a 5.96 MeV energy loss from the projectile and a 9.51 MeV loss from the recoil straggling. This would give the average recoil kinetic energy of around 146 MeV for beam energies of 357 MeV. As described earlier in section 4.2, there is also a small energy spread of the beam of $\pm 1\%$, meaning the projectile energy for this value would vary between 361 MeV and 353 MeV before even hitting the target.

7.2. Charge state distribution

During the collection of these data, it was noted that the beam energy was considerably less than the desired amount, affecting the original predictions of the average charge state expected, amongst other parameters. The following data was collected notwithstanding, and details of the consequences are further discussed in section 8. The value of the stopping power, is more or less consistent with a 10% decrease in beam energy and the previous plot is still valid for the sake of these results.

For each experimental run, where each run had a different charge set to be its reference particle, three charge states were collected. Of these the two most centrally located in the MWPC were compared with one another. Table 7.1 below shows the raw number of counts collected for each run. The ratio of those two charge states from each run shows which is the more abundant state and table 7.2 gives the relative abundance of the higher charge with respect to the lower charge for each run.

Run (q_0)	Charge [q]	Number of counts
R35 (32.5)	33	3891
	32	9349
R37 (31.5)	32	18277
	31	37227
R38 (30.5)	31	22626
	30	39741
R39 (29.5)	30	18078
	29	24554

Table 7.1: Raw number of counts taken from spectrum data for four different runs. Each run defines its reference charge in brackets.

Charge state	Relative Intensity
q (32)	2.402 q (33)
q (31)	2.037 q (32)
q (30)	1.756 q (31)
q (29)	1.358 q (30)

Table 7.2: The relative abundance of the higher charge with respect to the lower charge for each run. The run order follows the same as that in table 7.1.

The final representation of the charge state distribution can be seen in figure 7.2. Essentially the number of counts can be any number as what is important here is the relative abundance to the next charge state. For this reason, the number of counts in run 35 (R35) was arbitrarily taken as standard, and the ratios calculated from that.

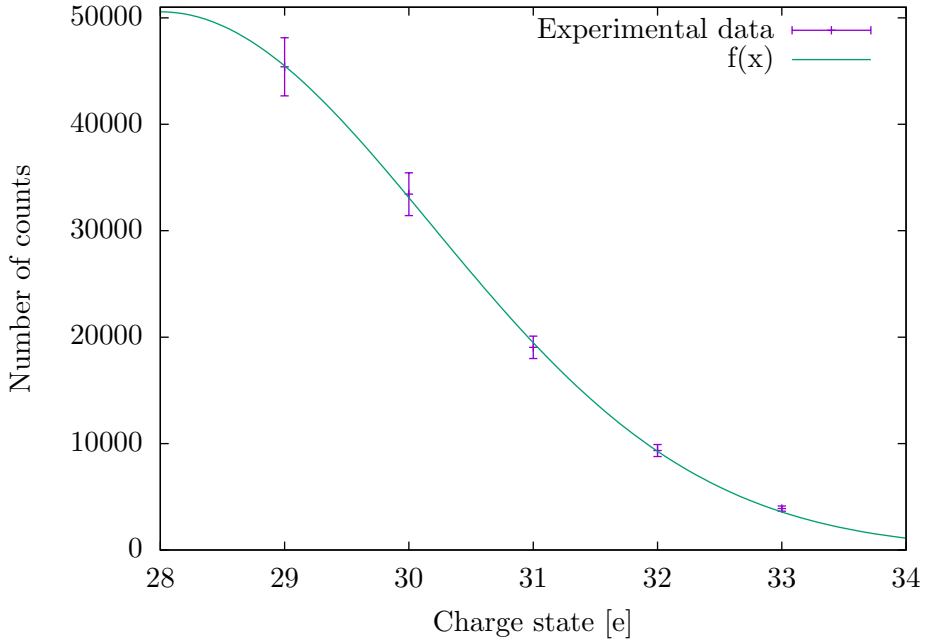

Figure 7.2: Final charge state distribution for ^{78}Kr on^{98}Mo reaction at beam energy of 357 MeV. The distribution is fitted to a Gaussian function.

Finally, the results were fitted to the gaussian function:

$$f(x) = Ae^{-\frac{(x-\mu)^2}{2\sigma^2}} \tag{7.1}$$

Where μ is the mean charge state and σ the standard deviation, which is proportional to the full width at half maximum (FWHM): FWHM $= 2\sqrt{2\ln 2}\sigma$. A is the amplitude of the gaussian and is related to σ:

$$A = \frac{1}{\sigma\sqrt{2\pi}} \tag{7.2}$$

Parameters were as follows for the fit:

Parameter	Value	Error[%]
A	50613.60	3.68
σ	2.17	4.45
μ	27.99	0.68

Table 7.3: Results from fitting a Gaussian function to the experimental data

The FWHM $= (5.109 \pm 0.22)q$. The width of the distribution, as calculated by equation 4.2 was $d_{\bar{q}} = (1.8 \pm 0.36)q$. The problem with the latter calculation, is that it does not include the additional contribution from the beam energy straggling through the target. This broadens the velocity range of the recoil and therefore the final width of this distribution. It does, however give an implication of how much broadening is caused by the beam.

The function fits the data points very well to within the experimental error. Measurements for only one side of the distribution were collected. Aside from the beam energy being lower than required, during this analysis it was also noted that the initial estimates for the average energy and charge state of the CN had been calculated too crudely. Namely, the stopping power of the recoil in the target results in a lower kinetic energy than that initially assumed. A combination of both issues consequentially meant there was a reduction in the value for $\bar{q}$, than what was initially expected.

7.2.1 Errors

Standard error on the number of counts was taken as $\sqrt{n}$. A contributing factor to this error is the systematic accuracy of the gating procedure. The error in how the gate was selected was initially calculated to be around 11%, however this was considered as a large overestimate and a more appropriate value of 6% was adopted. The error was estimated by taking several gates on one charge state and finding the standard error on the mean. Thus the real error of all data points is $\sqrt{n}$ plus 6% of the total number of counts.

8. Discussion

Initial test runs provided a preliminary insight to the recoil nuclei that were being collected. During these runs it was noted that the beam energy was significantly lower than expected. In the early stages of these runs, the target itself was changed as originally it was planned to use ^{92}Mo as the target as opposed to ^{98}Mo. Higher energies are required to overcome the Coulomb barrier for ^{92}Mo. The required energy to overcome the Coulomb barrier in the laboratory frame sits 15 MeV lower for ^{98}Mo than for ^{92}Mo, making it a good substitute.

During those test runs it was also noted that an accumulation of two masses; A = 172 and 173 were being collected in an approximately equal ratio, as seen in figure 6.3. Assuming the calculations from PACE4 are somewhat accurate, the theoretical results indicate that at the expected energy of 357 MeV the A=172 mass would be around 10 times more abundant than for A=173, with the ratio rapidly becoming more comparable as the beam energy decreases. Looking at figure 3.3, masses A = 172 and 173 are produced in almost equal abundance at around the beam energy of 335 MeV, therefore it can be inferred that either the real beam energy was closer to this value, or energy loss due to straggling in the target played a more important role than initially considered. During the course of the analysis, it seemed that both reasons contribute, however the latter having much less significance.

The lower charge state distribution collected is due to the recoil having a lower kinetic energy than anticipated. Figure 7.1 shows how the final kinetic energy of the recoil, after the target, is affected by the depth at which it was created inside the target. Since the stopping power of the recoil is higher than that of the projectile, it is clear that the earlier the CN is constructed, the greater the recoil energy loss and the lower its final kinetic energy will be.

The average charge state as approximated by a Gaussian fit, was given as 27.99 ± 0.20. Working backwards from equation 4.1, this implies that the real beam energy would be just at the Coulomb barrier, but this is also a very crude estimate to make, and it seems rather unlikely that it would be the case that the beam energy was so low. As there is no data point for q=28, it is difficult to say where the maximum of the distribution is and it can be reasonable to assume the average may actually be somewhere between q = 28 and 29.

For example, if an average charge state of 29 is assumed, a much more reasonable beam energy estimate is obtained of ≈330 MeV, already including average losses from straggling. It should be noted that these calculations are only rough approximations, as it is difficult to precisely determine the real beam energy at this point. Several other reasons could contribute to the lower $\bar{q}$ value including underestimates of the SRIM calculations for the stopping power, and inaccurate cross-section calculations as given by PACE4. It is also possible that the non-optimal energy selection of the reference particle has had an impact on the results. For the electrostatic deflector, a reference energy of $E_{\mathrm{k}} = 150\,\mathrm{MeV}$ was selected, whereas, when looking at figure 7.1 a reference energy of $E_{\mathrm{k}} = 146\,\mathrm{MeV}$ would have been more appropriate. Since there is a relation between energy and charge, as described by equation 5.3, the distribution can then be biased towards collecting a slightly lower charge state.

Further theoretical results from the PACE4 program demonstrates that nearly all recoils are within a 3° angular distribution of the central axis meaning that most of the ^{173}Os recoils are within the acceptance of MARA. Thus, it would seem that the maximum possible yield that can be obtained with this type of reaction is possible with MARA, if we assume those calculations to be accurate.

For the original reaction where ^{92}Mo was the target, the aim was to compare the results to the same experiment performed at FMA in 1997 [28]. Although not directly comparable with the results presented here, the number of charge states detected in the focal plane at FMA is the same order as what can be achieved with MARA.

Finally, it is noteworthy that after these commissioning experiments is was clear that the calculated values of the electrostatic deflector did not properly centralise the particles along the optical axis. Hence, since then the value of the deflector has been increased by 1.5% which now centralises the reference particle as desired. Reasons why this is the case are not clearly understood, but it should be noted for future experiments that this should be taken into account.

9. Conclusion

This thesis work was a study of the charge state distribution of the fusion evaporation reaction of ^{78}Kr on ^{98}Mo products, at an expected beam energy of 357 MeV. During the analysis it became apparent that the beam energy was considerably lower than initially assumed, affecting the predicted value of the average charge of the distribution. It can be assumed, that the real beam energy was closer to 335MeV, as a crude approximation. Analysis on the stopping power of both the recoils and beam in the target have been taken into account, and although they are contributing factors they are not enough to be solely responsible for the reduced charge state produced. Furthermore, more accurate calculations of projectile and recoil stopping power before the experiment could improve the $\bar{q}$ prediction. As such, selection of the electric and magnetic fields values could be more accurately chosen for the reference particle giving better statistics.

The results could be improved if more charge states were collected to have both sides of the Gaussian distribution to obtain a better fit. The small number of data points made it difficult to pinpoint more precisely where the average charge state of the distribution is. Aside from a lower $\bar{q}$, results fit nicely to an expected Gaussian profile to within experimental errors and it can be successfully seen which charge states will give a maximum yield through MARA within its acceptance, for this reaction.

Bibliography

[1] Y. A. Berezhnoye, *The quantum world of nuclear physics*, World Scientific Publishing Co. Pte. Ltd. Singapore, p115, 2005

[2] M.Satake, *An introduction to nuclear chemistry*, Discovery Publishing House, New Delhi, India, p156, 2003

[3] J. Partanen, J. Uusitalo, J. Sarén et al. *Commissioning of MARA vacuum-mode recoil mass separator*, University of Jyväskylä, Finland, 15/09/2015

[4] R.Singh and S.N.Mukherjee, *Nuclear Reactions*, New Age International (P) Ltd. New Delhi, India, p117, 2009

[5] Prof. Lee L. Riedinger, `http://www.phys.utk.edu/expnuclear/gammaspec.html`, The University of Tennessee, July 2016

[6] A.Gavron, `http://lise.nscl.msu.edu/pace4.html`, April 2016

[7] E.A. Khaleel, *Study of fusion evaporation channels in the* $^{18}\mathrm{O} + ^{18}\mathrm{O}$ *reaction at 65MeV*, Masters Thesis, Stellenbosch University, South Africa, p7-9, 2011

[8] J.Lilley, *Nuclear physics: principles and applications*, John Wiley & Sons Ltd. Inc. West Sussex, England, p87, p109, 2001

[9] W.S.C. Williams, *Nuclear and particle physics*, Oxford University Press, Oxford, UK, p12 1991

[10] Kenneth S. Krane, *Introductory Nuclear Physics*, John Wiley & Sons Ltd Inc. New Jersey, US, p49, p56 1987

[11] R.Bass, *Fusion of heavy nuclei in a classical model*, Nuclear Physics A 231 (1974) 45

[12] J.M.Blatt and V.F. Weisskopf, *Theoretical nuclear physics*, Springer-Verlag New York Inc. p367-372, 1979

[13] Daniel J. Blumenthal, *A Study of Cooling Following Nuclear Reactions*, PhD Thesis, Yale University, p15, 1994

[14] W. Loveland, http://oregonstate.edu/instruct/ch374/ch418518/Chapter%2010%20NUCLEAR%20REACTIONS.pdf, Oregon State University, Nuclear Chemistry Group, April 2016

[15] G. Choppin et al. *Radiochemistry and nuclear chemistry*, Elsevier Inc. Oxford, UK, p322, 2013

[16] Jan Sarén, *The ion-optical design of the MARA recoil separator and absolute transmission measurements of the RITU gas-filled recoil separator*, PhD Thesis, University of Jyväskylä, 2011

[17] Jan Sarén, *Private Communication*, University of Jyväskylä.

[18] Ahmad A. Kamal *1000 solved problems in modern physics*, Springer-Verlag Berlin Heidelberg, p369, 2010

[19] A. Kamal, *Nuclear physics*, Graduate Texts in Physics, Springer Berlin Heidelberg, p485, 2014

[20] P. Regant, http://personal.ph.surrey.ac.uk/p̃hs1pr/lecture_notes/nuc_expt_phr03.pdf, University of Surrey, p11, 2003

[21] G. Schiwetz & P.L. Grande, *Improved charge state formulas*, Nucl. Instr. and Meth. B 175-177 (2001) 125

[22] V.S. Nikolaev & I.S. Dmitriev, *On the equilibrium charge distribution in heavy element ion beams*, Phys. Lett. A 28 (1968) 277

[23] G.F.Knoll *Radiation detection and measurement*, John Wiley & Sons Ltd. Inc. p30, 2010

[24] Juha Uusitalo, *Private Communication*, University of Jyväskylä.

[25] James F. Ziegler, http://www.srim.org, April 2016

[26] P Rahkila. *Grain - A Java Data Analysis System for Total Data Readout*, University of Jyväskylä, Elsevier Inc. 2008

[27] S. Wolfram, `https://www.wolframalpha.com/input/?i=density+98Mo`, Wolfram Research, March 2016

[28] C.N. Davis et al. *New proton radioactivities* ^{165,166,167}Ir *and* ^{171}Au, Phys. Rev. C 55, 2255 (1997)